How Northern High-Latitude Volcanic Eruptions in Different Seasons Affect ENSO

Weiyi Sun,[a] Bin Wang,[b,c] Jian Liu,[a,d,e] Deliang Chen,[f] Chaochao Gao,[g] Liang Ning,[a]
and Lin Chen[h,b]

[a] *Key Laboratory for Virtual Geographic Environment, Ministry of Education, Jiangsu Provincial State Key Laboratory
Cultivation Base of Geographical Environment Evolution, Jiangsu Center for Collaborative Innovation in Geographical
Information Resource Development and Application, and School of Geography Science, Nanjing Normal University, Nanjing, China*
[b] *Department of Atmospheric Sciences and Atmosphere–Ocean Research Center, University of Hawai'i at Mānoa, Honolulu, Hawaii*
[c] *Earth System Modeling Center, Nanjing University of Information Science and Technology, Nanjing, China*
[d] *Jiangsu Provincial Key Laboratory for Numerical Simulation of Large Scale Complex Systems, School of Mathematical
Science, Nanjing Normal University, Nanjing, China*
[e] *Open Studio for the Simulation of Ocean-Climate-Isotope, Qingdao National Laboratory for Marine Science and
Technology, Qingdao, China*
[f] *Regional Climate Group, Department of Earth Sciences, University of Gothenburg, Gothenburg, Sweden*
[g] *College of Environmental and Resource Science, Zhejiang University, Hangzhou, China*
[h] *Key Laboratory of Meteorological Disaster, Ministry of Education/Joint International Research Laboratory of Climate and
Environmental Change/Collaborative Innovation Center on Forecast and Evaluation of Meteorological Disasters,
Nanjing University of Information Science and Technology, Nanjing, China*

ABSTRACT

The impact of northern high-latitude volcanic (NHV) eruptions on El Niño–Southern Oscillation (ENSO) is investigated based on ensemble simulations with the Community Earth System Model. The seasonality of the atmospheric circulation influences the NHV aerosol dispersion, causing stronger (weaker) Northern Hemisphere cooling after the January and April (July and October) eruptions. ENSO's response is found to be more dependent on NHV eruption seasons than that on tropical eruption seasons. The January eruption causes an El Niño in an eruption year [year (0) hereafter] while an El Niño occurs in year (1) after the October eruption. No significant El Niño occurs after the April (July) eruption. A diagnostic analysis reveals that these El Niños' developments are attributed to the positive zonal, meridional advective, and thermocline feedbacks, triggered by the western Pacific westerly anomalies. The anomalous North Pacific cyclone (NPC) and Asian monsoon are key systems to excite anomalous westerlies, which are caused by the NHV-induced midlatitude cooling and Eurasian continent–North Pacific thermal contrast. After the January eruption, the anomalous NPC develops in early summer and connects with a weakened Asian summer monsoon, which excites anomalous westerlies over the Indo-western Pacific, activating the Bjerknes feedback. For the October eruption, the anomalous NPC and enhanced East Asian winter monsoon bring cold air to the Maritime Continent and warm the subtropical central North Pacific through surface heat flux exchange, exciting the westerly anomalies. These results suggest that the strong dependence on the seasonal timing of NHV should be a critical element of data–model comparisons.

1. Introduction

El Niño–Southern Oscillation (ENSO) plays a dominant role in the interannual variability of tropical climate (Webster et al. 1998) and profoundly influences the entire Earth through atmospheric teleconnections, modulating floods, droughts, tropical cyclone activity, and other extreme climate events (Wallace and Gutzler 1981; Ropelewski and Halpert 1987; Wang et al. 2000; Ning and Bradley 2015). El Niño and La Niña are the warm and cold phases of the ENSO cycle (2–7 years). However, they are not mirror images and exhibit asymmetries in their spatial–temporal evolution and intensity (Philander 1985; Choi et al. 2013; Wu et al. 2018).

Volcanic eruption is an important external forcing that contributes greatly to abrupt climate changes on multiple time scales (e.g., Robock 2000; Liu et al. 2013; Ning et al. 2017). Large volcanic eruptions inject sulfur

Denotes content that is immediately available upon publication as open access.

Supplemental information related to this paper is available at the Journals Online website: https://doi.org/10.1175/JCLI-D-18-0290.s1.

Corresponding author address: Jian Liu, jliu@njnu.edu.cn

gases into the stratosphere, which are then converted into sulfate aerosols. These aerosols warm the stratosphere by absorbing both solar and terrestrial radiation and cool the surface by scattering part of solar radiation back to space (Robock 2000).

Previous studies of long-term paleoclimate data suggest that the large tropical volcanic eruptions can induce an El Niño–like state or increase the occurrence probability of El Niño events (Adams et al. 2003; McGregor et al. 2010; Li et al. 2013). Processes by which tropical volcanic eruptions influence the ENSO have been proposed and discussed using numerical experiments with coupled climate models. Some studies suggest that, under a tropical volcanic forcing, the larger land area in the Northern Hemisphere results in a stronger cooling than in the Southern Hemisphere, thereby shifting the intertropical convergence zone (ITCZ) southward and inducing anomalous westerlies in the equatorial Pacific as well as El Niño events (Lim et al. 2016; Stevenson et al. 2016; Pausata et al. 2015b). Other researchers find that the El Niño events can be excited by the dynamical thermostat mechanism (Mann et al. 2005; Emile-Geay et al. 2008; McGregor and Timmermann 2011; Maher et al. 2015; Predybaylo et al. 2017) and by anomalous equatorial westerlies due to the land–sea thermal contrast over the Maritime Continent (Ohba et al. 2013; Sun et al. 2018). In addition, Khodri et al. (2017) propose that tropical volcanic eruptions cool tropical Africa and weaken the West African monsoon, thus inducing eastward propagating atmospheric Kelvin waves that excite anomalous westerlies in the equatorial Pacific and increase sea surface temperature (SST) over the eastern Pacific.

Compared with tropical volcanic eruptions, northern high-latitude volcanic (NHV) eruptions have received less attention. Nevertheless, some researchers have highlighted the important effects of high-latitude eruptions, which can significantly change pole-to-equator temperature gradients and influence the atmospheric general circulation (e.g., Robock 2000; Shindell et al. 2004; Oman et al. 2005; Kravitz and Robock 2011). Strong high-latitude eruptions, such as the Laki eruption in 1783, weaken the African, Indian, and East Asian monsoons (Oman et al. 2006a), leading to severe famines (Thordarson and Self 2003). Recently, the state-of-the-art climate models have been used to examine the tropical climate's response to the Northern Hemisphere volcanic forcing. Using GISS-E2 and the Community Earth System Model (CESM), Colose et al. (2016) find that the ITCZ moves southward after the Northern Hemisphere volcanic eruptions. Further, Stevenson et al. (2016) suggest that the probability of El Niño is greater following the northern eruptions. Liu et al. (2016, 2017) also found that the Northern Hemisphere monsoon precipitation is suppressed and the El Niño–like state occurs after the Northern Hemisphere eruptions by proxy data and CESM.

These studies (Colose et al. 2016; Stevenson et al. 2016; Liu et al. 2016, 2017) use the volcanic forcing derived from the ice core reconstruction by Gao et al. (2008). The optical depth of this forcing data is consistent with satellite observations and the global climate model (GCM) calibrated calculation (Stenchikov et al. 1998) of the Mount Pinatubo eruption in 1991. Using NorESM1-M ensemble simulations, Pausata et al. (2015a,b) analyze the impact of the 1783 Laki eruption in Iceland on ENSO. They find an El Niño–like anomaly occurred after the Laki eruption, which is consistent with observations (the Laki eruption in 1783 and Katmai eruption in 1912) (Rayner et al. 2003; Cook et al. 2010). They proposed that the El Niño–like anomaly is caused by the high-latitude volcanic-induced cooling that pushes the ITCZ southward, enhancing the anomalous westerlies over the equatorial Pacific. In a follow-up study, Pausata et al. (2016) test the sensitivity of the tropical Pacific under high-latitude volcanic forcing to different initial states (El Niño, La Niña, and neutral state), showing that the El Niño–like anomalies occur in the winter after the NHV eruption. Their amplitudes are determined by the initial state of the tropical Pacific.

To better predict the high-latitude volcanic effects on abrupt climate changes and ENSO development, the seasons of volcanic eruption occurrence must be taken into consideration, although few researchers have thus far considered this. As the starting seasons of many historical volcanic eruptions are unknown, researchers usually assume eruptions occur during the same season (e.g., Man et al. 2014; Otto-Bliesner et al. 2016). However, some recent studies show that the atmospheric circulation and ENSO responses are different when tropical volcanic eruptions occur in different seasons (Stevenson et al. 2017; Predybaylo et al. 2017). Equatorial eruptions also have an asymmetric forcing due to, for example, seasonal variations of insolation and the extremely large eruptions could maintain a strong forcing all year long decreasing the role of timing of an eruption. Thus, for high-latitude eruptions, we anticipate that the influences of differences in eruption seasons can be even stronger, due to larger seasonal variations in insolation and sulfate aerosol deposition rates (Kravitz and Robock 2011).

Therefore, the primary target of this study is to assess the effects of seasonal variations of NHV eruptions on the ENSO evolution. To the best of our knowledge, no study to date has investigated these impacts in detail.

Here ENSO responses to NHV eruptions in four different seasons are simulated by CESM.

The paper is organized as follows. Section 2 introduces the model, experimental design, and method. Section 3 describes the overall climate and the ENSO responses to the NHV eruptions. Section 4 analyzes the physical processes responsible for El Niño's development after NHV eruptions. Section 5 pinpoints how the NHV-induced atmospheric changes trigger El Niño's development, and a new "anomalous North Pacific cyclone and Asian monsoon" triggering mechanism is proposed. Section 6 presents the discussion and the conclusions are shown in section 7.

2. Model and analysis method

a. Model and experiments

The model used in this study is CESM with the Parallel Ocean Program version 2 (POP2) and the Community Atmosphere Model, version 4 (CAM4) (Neale et al. 2013). The performance of CESM is verified by numerous researchers (e.g., Wang et al. 2015; Ning and Bradley 2016; Otto-Bliesner et al. 2016; Ning et al. 2018). In this study, the low-resolution version (T31_g37, which is equivalent to $3.75° \times 3.75°$ in the atmosphere and land components) is used to carry out the long time integration, given the limited computing resources at our disposal. CAM4 has 48 grid points in latitude, 96 grid points in longitude, and 26 vertical levels, while POP2 has 116 grid points in latitude, 100 grid points in longitude, and 60 vertical levels.

A 2000-yr control simulation (Ctrl) is performed with all external forcing fields fixed at 1850, after a 400-yr preindustrial spinup run (Wang et al. 2015). The NHV experiments contain a 14-member ensemble simulation (integrated for 10 years) for each eruption experiment using the prescribed volcanic forcing initiated with different years adopted from Ctrl. Year (0) represents the volcanic eruption year, while year (1) denotes the first year after volcanic eruption. Following Pausata et al. (2016) and Predybaylo et al. (2017), we add the volcanic forcing in four seasons in year (0), and we choose the ENSO peaks during DJF (0/1) in the Ctrl experiment as the initial condition. From the observed Niño-3.4 index (5°S–5°N, 170°–120°W; HadSST; Rayner et al. 2003) during the DJF season from 1901/02 to 2017/18, the probabilities of El Niño (Niño-3.4 index > 0.5°C), neutral (−0.5°C < Niño-3.4 index < 0.5°C), and La Niña (Niño-3.4 index < −0.5°C) occurrence are 30.0%, 39.2%, and 30.8%, respectively. To detect the volcanic effects under a more realistic condition, we selected 4 El Niño cases, 6 neutral cases,

and 4 La Niña cases based on the real probabilities of ENSO's occurrence as the initial conditions. Additionally, we select 14 members to form a no-volcano ensemble. The 14 members selected in the Ctrl are the same years as the volcanic forcings were placed in the NHV experiment.

The spatial–temporal distribution of the monthly mean volcanic forcing is produced according to the stratospheric transport parameterization proposed by Grieser and Schönwiese (1999) and adapted by Gao et al. (2008). The Northern Hemisphere is divided into eight equal-area latitude belts (three in the tropics, four in the midlatitudes, and one in high latitude). The horizontal spread of aerosols within the low stratosphere is parameterized using information obtained from the studies of stratospheric mass transport (Grieser and Schönwiese 1999) and uncertainties are contained in the estimates. The original values are modified to reflect the seasonal dependence of aerosol dispersion and polar depositions (Table 2 in Gao et al. 2008). The global total amount of stratospheric sulfate aerosol (32 Tg) is similar to the magnitude of the 1991 Pinatubo (30 Tg), but it was injected in the most northern midlatitude band of 64°N (similar to the 1783 Laki eruption). This volcanic forcing is chosen because it is difficult for weak volcanic forcing to obtain significant climate impact. Further, these medium-size volcanic eruptions are more frequent than the larger ones and are therefore more representative over the past 2500 years (Kravitz and Robock 2011; Kravitz et al. 2015; Sigl et al. 2015).

The idealized eruption scenarios begin on 15 January (JAN), 15 April (APR), 15 July (JUL), and 15 October (OCT), respectively, and the maximum aerosol mass is reached 4 months after the eruptions (Fig. 1). This 4-month aerosol buildup was observed after the 1991 Pinatubo eruption (Guo et al. 2004). For the January and April eruptions, aerosol loading is stronger in the high latitudes and peaks in spring and early summer, compared with the July and October eruptions (Fig. 1). This is because the high (low) exchange rate of sulfate aerosols from the extratropics to the polar region is mainly caused by the polar vortex in boreal summer (winter) in the Northern Hemisphere (Grieser and Schönwiese 1999; Gao et al. 2008). The seasonal volcanic forcings are similar to previous model runs (Fig. 5 in Kravitz and Robock 2011). We also compare our volcanic forcing with the 1912 Katmai eruption from Ammann et al. (2003) and Sato et al. (1993) and the GISS ModelE results (Fig. 4 in Oman et al. 2006b). Observations and ModelE results indicate that the majority of the volcanic forcing remain north of 30°N, and a
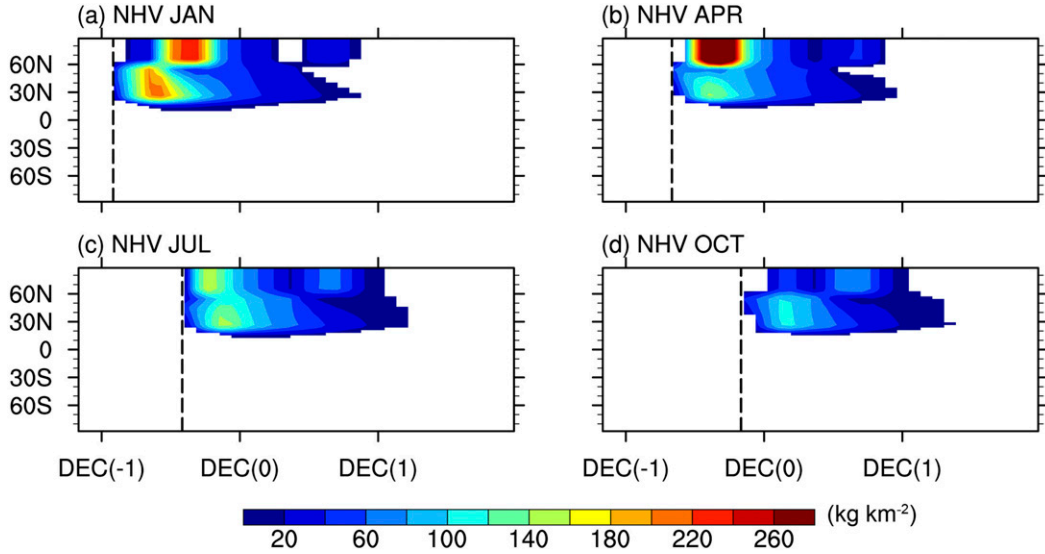
FIG. 1. Zonally averaged aerosol column density (kg km^{-2}) for the NHV eruption in (a) January, (b) April, (c) July, and (d) October. The vertical dashed lines represent the eruption months.

certain amount of it is transported to south of 30°N latitude, which is similar to the forcing in this study.

b. Method

The anomalies in each NHV experiment are calculated as the departures from the corresponding unperturbed counterpart (NHV − Ctrl). We use a null hypothesis of no changes in SST, surface temperature, SLP, and winds following the NHV eruption. Uncertainties in the anomalies were estimated using a block-bootstrap procedure (Kunsch 1989; Emile-Geay et al. 2016) with 5000 draws. The block length was set at 2 years for the interannual difference.

The false discovery rate (FDR) procedure is also used to control the proportion of falsely rejected null hypotheses out of all rejected null hypotheses (Benjamini and Hochberg 1995). This has been illustrated quite pedagogically in climate science by Ventura et al. (2004), and its importance was recently pointed out by Hu et al. (2017). Here we set $q = 5\%$ to guarantee that 5% or fewer of the locations where the null hypothesis is rejected are false detections on average. The followings are the processes of the FDR procedure (Benjamini and Hochberg 1995):

1) Calculate p values at all m locations;
2) Rank the p values $p_{(i)}$ in increasing order: $p_{(1)} \leq p_{(2)} \leq \cdots \leq p_{(m)}$;
3) Define k as the largest i for which $p_{(i)} \leq q(i/m)$;
4) Reject hypotheses at locations $i = 1, 2, \ldots, k$.

In this study, a budget analysis of the mixed layer temperature anomaly is used to quantify the contributions of different processes to the El Niño development. This equation can be derived as follows (Li et al. 2002):

$$\frac{\partial T'}{\partial t} = -(\mathbf{V}' \cdot \nabla \overline{T} + \overline{\mathbf{V}} \cdot \nabla T' + \mathbf{V}' \cdot \nabla T') + \frac{Q'_{\text{net}}}{\rho C_p H} + R$$

$$= -\left[\left(\frac{u' \partial \overline{T}}{\partial x} + \frac{\overline{u} \partial T'}{\partial x} + \frac{u' \partial T'}{\partial x} \right) \right.$$
$$+ \left(\frac{v' \partial \overline{T}}{\partial y} + \frac{\overline{v} \partial T'}{\partial y} + \frac{v' \partial T'}{\partial y} \right)$$
$$\left. + \left(\frac{w' \partial \overline{T}}{\partial z} + \frac{\overline{w} \partial T'}{\partial z} + \frac{w' \partial T'}{\partial z} \right) \right] + \frac{Q'_{\text{net}}}{\rho C_p H} + R,$$

where the overbars and primes indicate climatological and anomalous quantities, respectively; T denotes the mixed layer temperature; $\mathbf{V} = (u, v, w)$ represents the zonal and meridional currents, and upwelling velocities, respectively; $\nabla = (\partial/\partial x, \partial/\partial y, \partial/\partial z)$ represents the three-dimensional gradient operator; $u' \partial \overline{T}/\partial x$, $v' \partial \overline{T}/\partial x$, and $w' \partial \overline{T}/\partial x$ denote the advection of mean temperature by anomalous ocean current velocities in three directions; $\overline{u} \partial T'/\partial x$, $\overline{v} \partial T'/\partial x$, and $\overline{w} \partial T'/\partial x$ represent the anomalous temperature by mean current velocities in three directions; and $u' \partial T'/\partial x$, $v' \partial T'/\partial x$, and $w' \partial T'/\partial x$ are the nonlinear terms in three directions. Also, Q_{net} denotes the net downward heat flux at the ocean surface; ρ ($= 10^3$ kg m^{-3}) is water density; C_p ($= 4000$ J kg K^{-1}) is the specific heat of water; H represents the mixed layer depth where ocean temperature is 0.8°C lower than the surface, following Saha et al. (2006) and Chen et al. (2017); and R denotes the residual term.
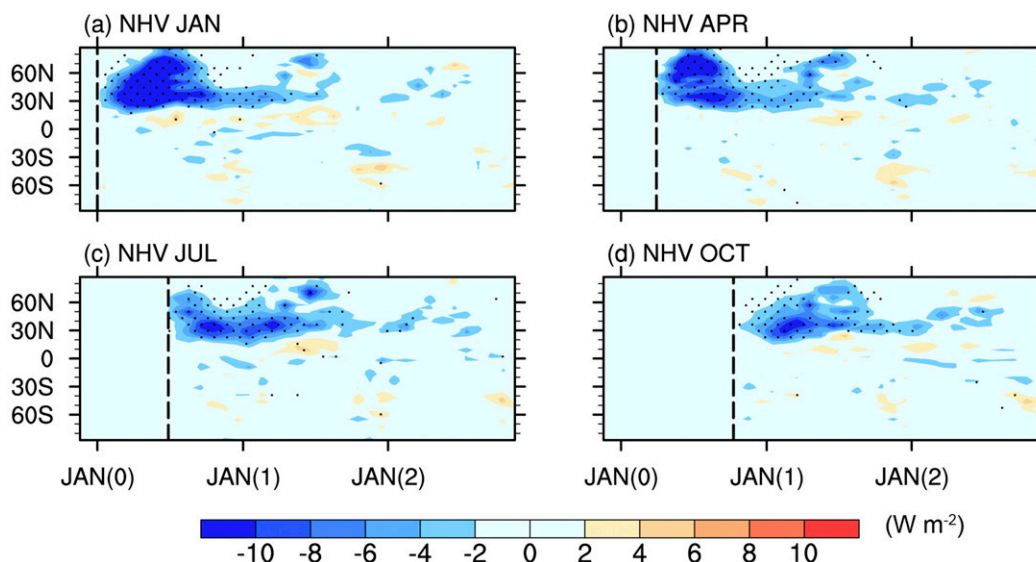
FIG. 2. Composite zonally averaged surface shortwave radiation anomalies (W m^{-2}) for the NHV eruption in (a) January, (b) April, (c) July, and (d) October, relative to the Ctrl ensemble mean. The vertical dashed lines represent the eruption months. The dots denote the anomalies are significant at the 5% test level.

3. Climate responses to the NHV eruptions

a. Surface shortwave radiation and temperature response to the NHV eruptions

Figure 2 shows the composite zonally averaged surface shortwave radiation anomalies after the NHV eruptions. In all cases, significant decreases of surface shortwave radiation appear shortly after each NHV eruption, which lasts for approximately one year, and the distribution is consistent with the sulfate aerosol loading. Because of the seasonality of the atmospheric circulation, the dispersion of the volcanic aerosol is different in each season, causing the larger reduction of shortwave radiation in the NH extratropical-to-polar region after January and April eruptions, compared with the July and October eruptions. Meanwhile, stronger insolation in late spring and summer in the Northern Hemisphere strengthens the reduction of shortwave radiation after January and April eruptions. These global radiative responses are similar to previous results (Kravitz and Robock 2011).

The global temperature responses are shown in Fig. 3. The temperature decreases largely over the NH extratropical-to-polar region in the first boreal summer and fall after January and April eruptions, which last longer and exhibit greater pole-to-equator temperature gradients compared with the July and October eruptions. The cooling in the polar region is stronger during fall (Figs. 3a and 3b) and can last for a longer period, most likely due to the snow/albedo feedback.

b. ENSO response to NHV eruptions

The CESM can simulate the ENSO evolutions after volcanic eruptions well, confirmed by the proxies and observational data (Liu et al. 2016; Liu et al. 2017; Stevenson et al. 2017; Sun et al. 2018).

Figure 4 displays ensemble mean boreal winter SST anomalies [November to January (NDJ)]. There is no significant warming or cooling over the central-eastern Pacific in NDJ (0/1) and (1/2) in the Ctrl ensemble (Figs. 4a,b). A strong El Niño happens in the winter following the January eruption (Fig. 4c), whereas no significant warming appears after the April eruption (Fig. 4d). In the JUL experiment, the eastern Pacific SST does not change in the first winter (Fig. 4e), whereas weak positive SST anomalies occur over the eastern Pacific in the following winter (Fig. 4f). In the October ensemble, no warming occurs over the eastern Pacific in the first winter, but an El Niño occurs over the eastern Pacific in the second winter (Figs. 4g and 4h).

Figure 5 shows the anomalous NH extratropical temperature (30°–60°N, 180°–180°) and Niño-3.4 index in the NHV experiment. The ensemble mean anomalous Niño-3.4 index in Ctrl experiment is close to zero from JAN (0) to JUN (2) (Fig. 5b), which means that the selected no-volcano ensemble mean is adequate to serve as a reference to detect volcanic effects by comparison with the NHV experiment. The magnitude of the NH extratropical cooling is substantially influenced by eruption season (Fig. 5a). After a January eruption,
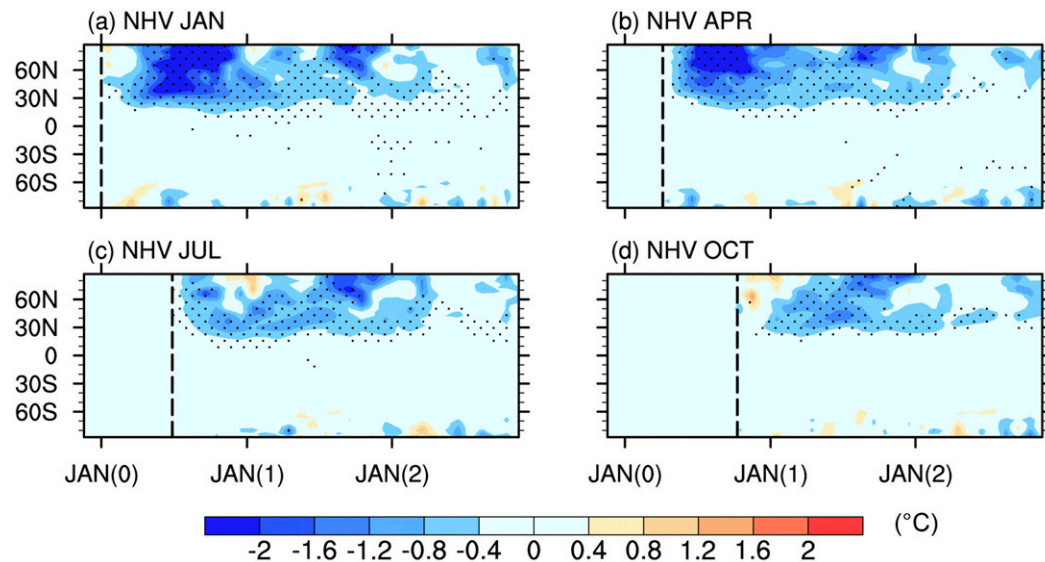
FIG. 3. As in Fig. 2, but for the surface temperature anomalies (°C).

strongest NH extratropical cooling occurs and the Niño-3.4 index increases after JUN (0) (Figs. 5a,c). At the end of year (0), an El Niño happens in the JAN experiment whereas insignificant warming occurs over the eastern

Pacific in the APR experiment (Figs. 6a and 6b). In year (1), the anomalous eastern Pacific warming rapidly decreases in the JAN experiment. Interestingly, the NH extratropical cooling is weaker in the OCT experiment
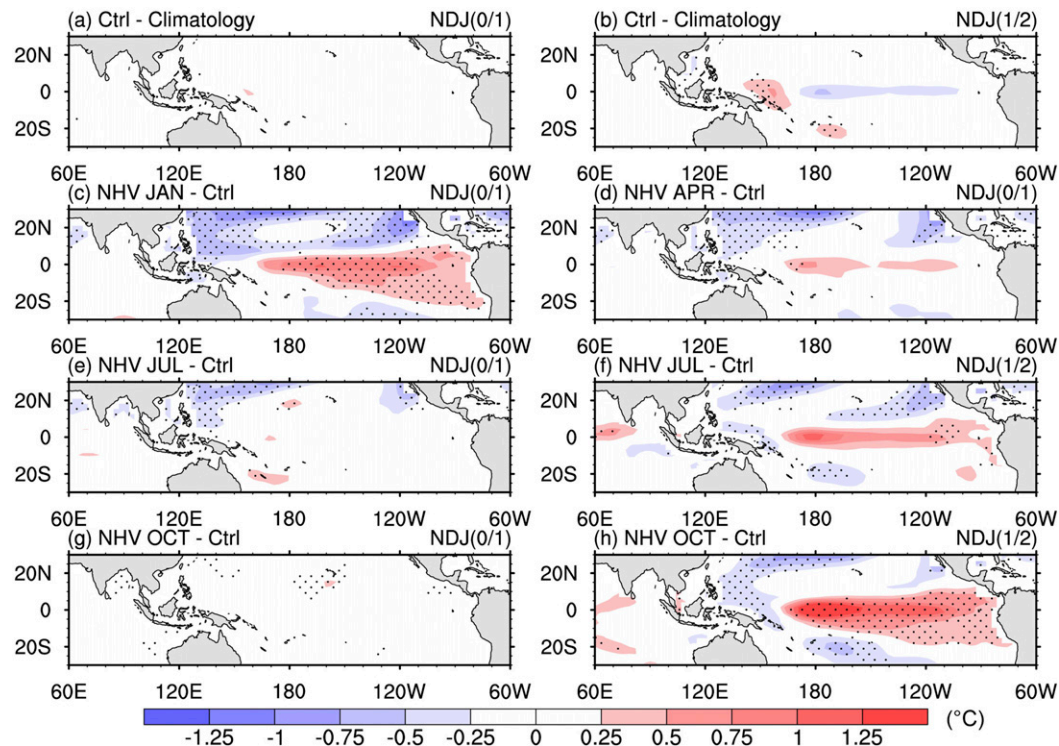

FIG. 4. Composite boreal winter SST anomalies (°C; November–January). (a),(b) Results in corresponding unperturbed ensemble in Ctrl, relative to the mean of the last 500 years. Results in the (c) JAN, (d) APR, (e),(f) JUL, and (g),(h) OCT experiments are relative to the Ctrl ensemble mean. Note that (a), (c), (d), (e), and (g) represent the first winter following the NHV, while (b), (f), and (h) represent the second winter after the NHV. The dots denote the anomalies are significant at the 5% test level.
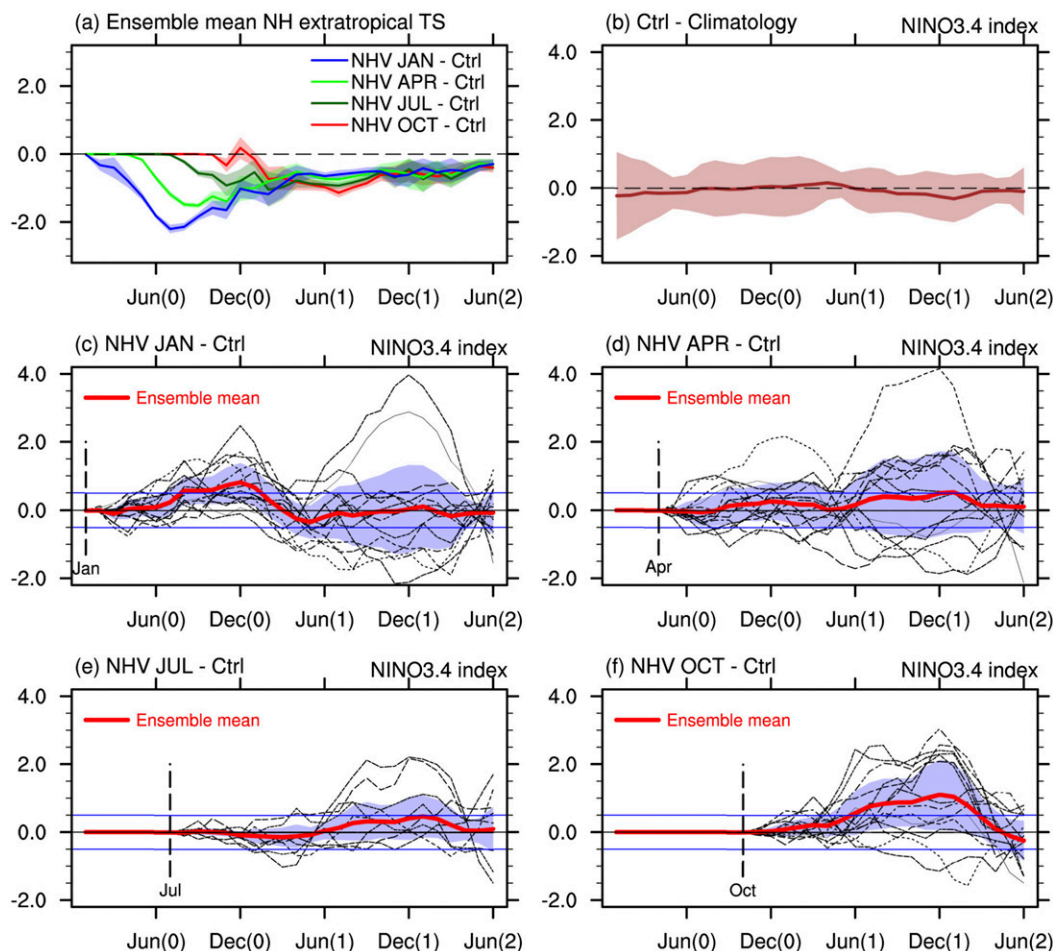
FIG. 5. (a) The time series of the simulated anomalous NH extratropical surface temperature (30°–60°N, 180°–180°) and anomalous SST (°C) over the Niño-3.4 region (5°S–5°N, 170°–120°W). (b) Ensemble mean anomalies in Ctrl, relative to the mean of the last 500 years. (c)–(f) The anomalies in the JAN, APR, JUL, and OCT experiments, respectively, relative to Ctrl ensemble mean. Red lines denote the ensemble mean anomalies. Shading represents twice the standard error of the mean. The vertical dashed lines represent the start of eruptions.

than that in the APR experiment, but a significant El Niño occurs at the end of year (1) in the OCT experiment (Figs. 5f and 6d).

We also simulate the NHV JUN (32 Tg) and 1783 Laki (93 Tg) eruption experiment 5 times (see Fig. S1 in the online supplemental material). A significant El Niño happens in the first winter after the Laki eruption, which is in agreement with the tree-ring data (Cook and Krusic 2004; D'Arrigo et al. 2011). This means that an El Niño occurs after the strong high-latitude volcanic eruption. However, no significant warming occurs after the June eruption (about one-third of Laki's size), which is consistent with the results in the summertime eruption (APR and JUL) experiments.

The differences between these El Niños' developments under the NHV eruption in different seasons are larger than that under the tropical eruptions

(Stevenson et al. 2017). Thus, the NHV eruption season is an important factor to influence the development of El Niño.

4. Diagnosis of mixed layer heat budgets

To investigate why the El Niño develops differently for the NHV eruptions in different seasons, a budget analysis of oceanic mixed layer temperature anomaly tendency (MLTA) averaged over the Niño-3.4 region is first conducted. In Fig. 7, the relative contributions of each of the terms affecting the MLTA during the El Niño developing phase are shown for two periods: June (0)–December (0) (Figs. 7a–c) and March (1)–December (1) (Figs. 7d,e). The budget analysis of the October ensemble during year (0) is not included because it only has 2 months after the eruption in year (0).
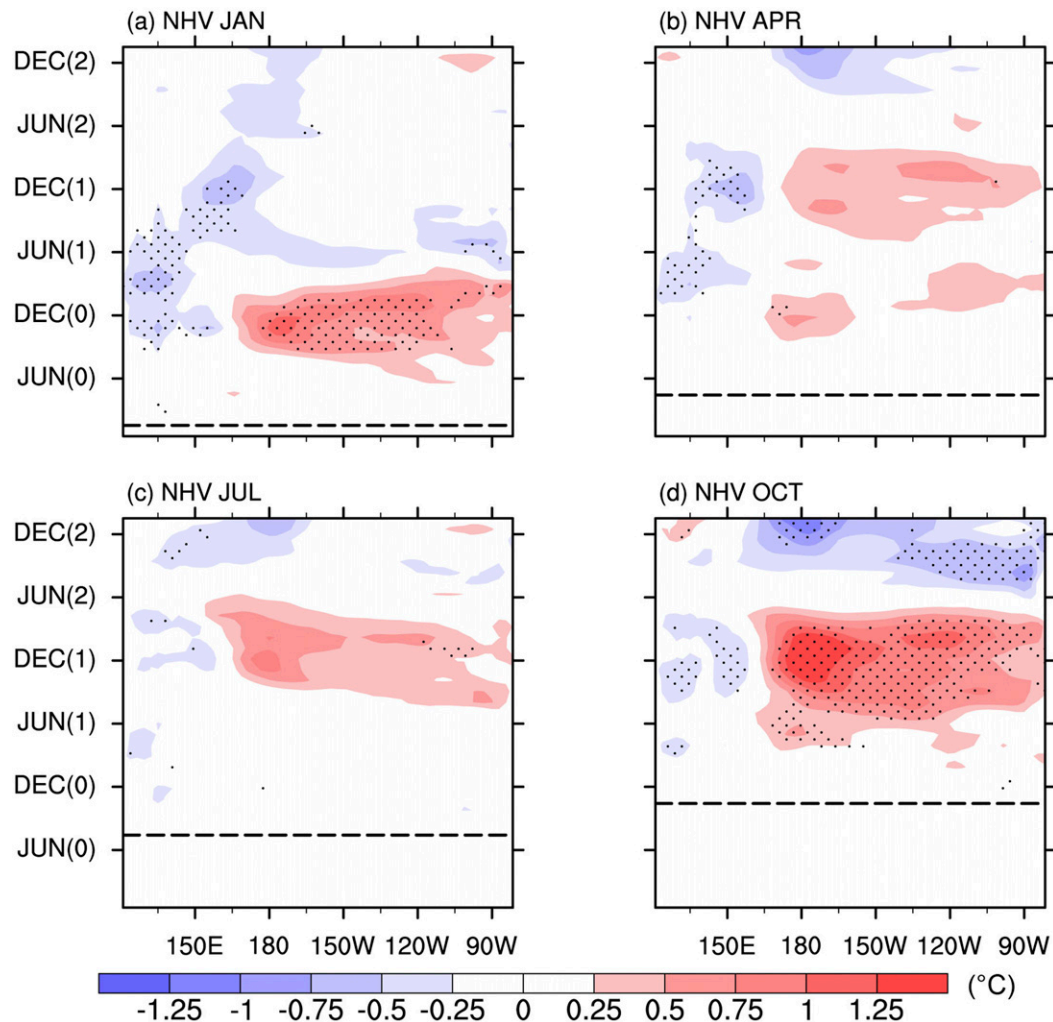
FIG. 6. Composite longitude–time plot of the SST anomalies (shading; °C) averaged over the equatorial Pacific (5°S–5°N) for the NHV eruption in (a) January, (b) April, (c) July, and (d) October. The horizontal dashed lines represent the eruption months. The dots denote the anomalies are significant at the 5% test level.

In year (1), we focus on the July and October ensembles because both of them have no significant SST change over the eastern Pacific in year (0) but exhibit different degrees of warming in year (1) (Fig. 5). The sustained growth of the Niño-3.4 index occurs at the spring (1) in the October ensemble. Therefore, we select the period of March (1)–December (1) as the El Niño developing phase in year (1) (Figs. 7d,e). Note that the estimated MLTA tendency (Fig. 7, bar 11) is close to the actual MLTA tendency (Fig. 7, bar 12), meaning that the mixed layer heat budget diagnosis results are credible.

The MLTA tendencies are 0.13°, 0.05°, and 0.00°C month^{-1} from June (0) to December (0) in the January, April, and July ensembles, respectively (Figs. 7a–c). In the January ensemble, the warming trend is largest, and zonal advection plays a crucial role during this period

(Fig. 7a). In particular, the advection of mean temperature by anomalous current ($-u'\partial\overline{T}/\partial x$; Fig. 7a, bar 1) contributes the most to the warming. At the same time, the meridional advective feedback ($-\overline{v}\partial T'/\partial y$; Fig. 7a, bar 8) and thermocline feedback ($-\overline{w}\partial T'/\partial z$, bar 5) also contribute to the MLTA tendency. The thermodynamic heat flux feedback [$Q'_{net}/(\rho C_p H)$; Fig. 7a, bar 10] is negative in the Niño-3.4 region with the positive MLTA tendency, which tends to damp the latter as expected. In the April eruption cases, the enhanced MLTA is also mainly due to the zonal advective feedback but its magnitude is much smaller than that in the January ensemble, leading to the weaker warming (Fig. 7b). However, for the July ensemble, all of the advection terms along with the thermodynamic heat flux, are close to zero in the following winter (Fig. 7c).
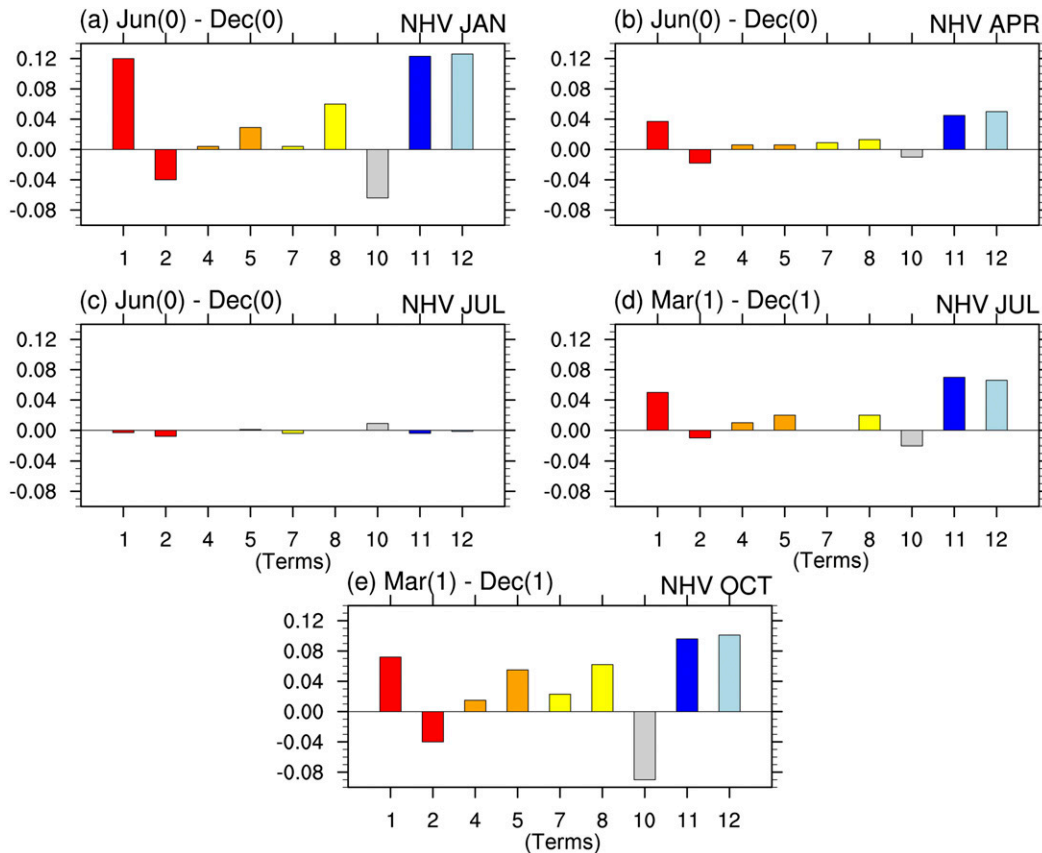
FIG. 7. Composite MLTA budget terms (ordinates are °C month^{-1}) during (a)–(c) June (0)–December (0) and (d),(e) March (1)–December (1) averaged over the Niño-3.4 region (5°S–5°N, 170°–120°W). Bar 12 represents the tendency in MLTA ($-\partial T'/\partial t$) and bar 11 is the sum of all 10 terms changes in the equation. The changes in the linear terms are as follows: $-u'\partial\overline{T}/\partial x$ (bar 1), $-\overline{u}\partial T'/\partial x$ (bar 2), $-w'\partial\overline{T}/\partial z$ (bar 4), $-\overline{w}\partial T'/\partial z$ (bar 5), $-v'\partial\overline{T}/\partial y$ (bar 7), $-\overline{v}\partial T'/\partial y$ (bar 8), and $Q'_{net}/(\rho C_p H)$ (bar 10).

During the period of March (1)–December (1), the MLTA tendencies are 0.06° and 0.10°C month^{-1} in the July and October ensembles, respectively (Figs. 7d and 7e). In the July ensemble, the zonal advective feedback (Fig. 7d) causes the insignificant warming over the eastern Pacific. Meanwhile, in the October ensemble, the increased MLTA is mainly caused by zonal, meridional advective, and thermocline feedbacks (Fig. 7e). The thermocline feedback in the OCT experiment is stronger than that in the JAN experiment. The thermodynamic heat flux also tends to slow down the warming trend, which is similar to the results for the January ensembles.

The feedbacks that affect MLTA tendency are all related to the surface wind stress over the equatorial Pacific (e.g., Su et al. 2010; Chen et al. 2015). Therefore, the examination of surface wind stress evolution is instrumental for understanding the MLTA change.

Figure 8 shows the evolution of the anomalous surface zonal wind stress (ZWS') and anomalous sea surface height (SSH'). The SSH' can also be approximately interpreted as a thermocline anomaly as they are positively related, especially over the eastern Pacific (Cane 1984). In the January ensemble, anomalous westerlies occur over the equatorial western Pacific after June (0), bringing warm water to the central Pacific, slackening the equatorial trade winds, and activating the Bjerknes feedback (Bjerknes 1969), which contributes to the eastern Pacific warming. The weakened equatorial wind stress also induces the positive SSH' over the equatorial eastern Pacific during the autumn and winter (Fig. 8a). The deeper anomalous thermocline depth can in turn lead to the enhanced equatorial upper-ocean zonal currents (u') through the geostrophic current (Su et al. 2010, 2014). At the same time, the thermocline becomes shallow (deep) in the west (east) Pacific, favoring the eastern Pacific warming by thermocline feedback, but this feedback happens in the late development of El Niño.

The largest temperature anomalies occur along the equator during June (0)–December (0) in the JAN
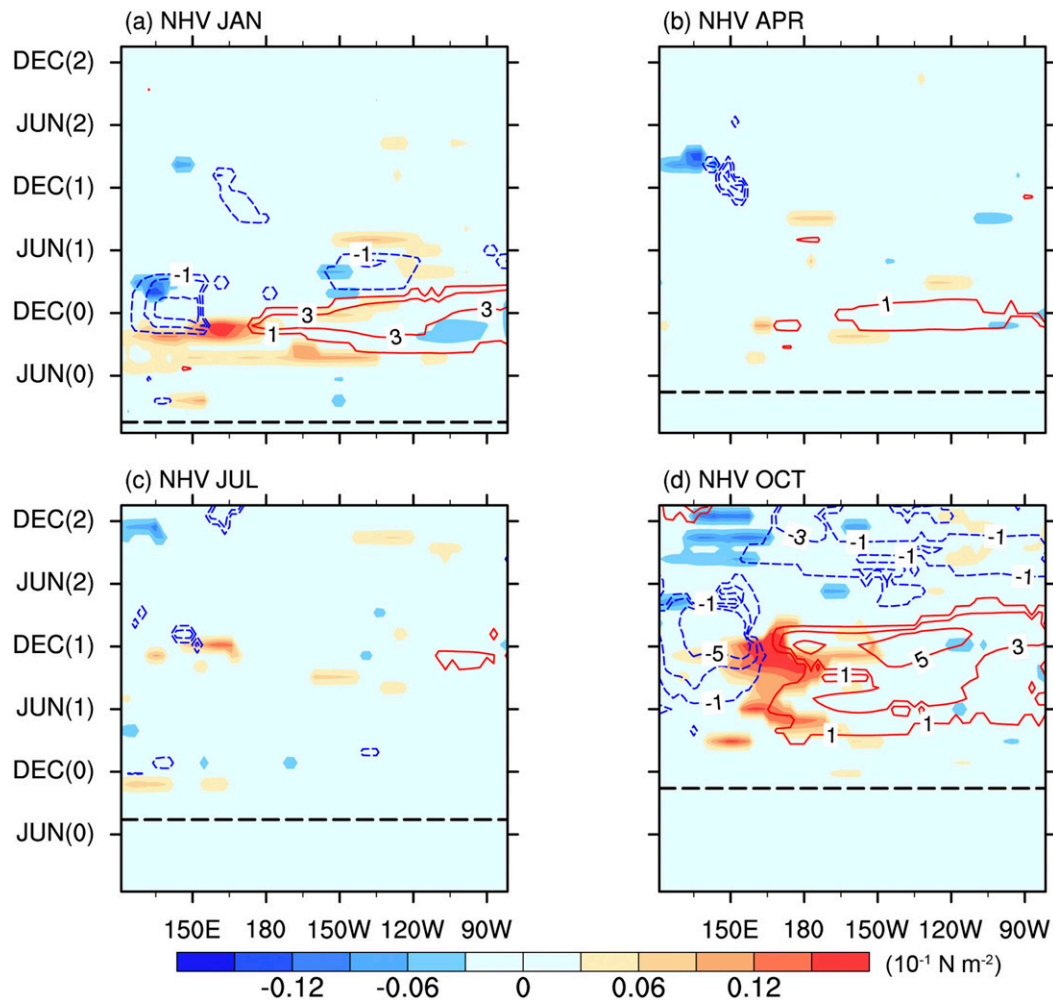
FIG. 8. Composite longitude–time plot of the surface zonal wind stress anomalies (shading; $10^{-1}\,\mathrm{N\,m^{-2}}$) and sea surface height anomalies (contours; cm) averaged over the equatorial Pacific (5°S–5°N) for the NHV eruption in (a) January, (b) April, (c) July, and (d) October. The horizontal dashed lines represent the eruption months. Only the anomalies significant at the 5% test level are shown.

experiment (Fig. S2a). The climatological mean meridional currents above the mixed layer depth are generated by Ekman flows. Under easterly wind stress the Ekman flow are always away from the equator, advecting warm water poleward, expanding and enhancing the warming over the Niño-3.4 region. This meridional advective feedback $(-\bar{v}\partial T'/\partial y)$ occurs above the mixed layer depth. The increase of zonal advective feedback leads the meridional advective feedback about 1 month, and the former is much greater than the latter (figure not shown). This implies that the meridional advective feedback acts to enlarge the warming.

In the April and July ensembles, no significant westerly anomalies occur over the equatorial Pacific (Figs. 8b,c), causing the small changes in u' and SSH'. Correspondingly, the zonal, meridional advective, and thermocline feedbacks are all weak (Figs. 7b–d). After the October eruption, the anomalous westerlies occur over the western Pacific during the spring in year (1) (Fig. 8d). Then the weakened wind stress is generated by the Bjerknes feedback and gradually extends eastward, leading to the zonal advective feedback. The positive SSH' prevails over the central-eastern Pacific from the spring (1) to winter (1), implying the enhanced thermocline feedback. When the warming develops over the eastern Pacific, the meridional advective feedback is induced (Fig. S2b), which tends to enlarge this warming.

In summary, after the January and October eruptions, the equatorial westerly anomalies over the western Pacific can initially activate the Bjerknes feedback through anomalous zonal advection, weakening the equatorial trade winds, and then enhance the advective feedbacks
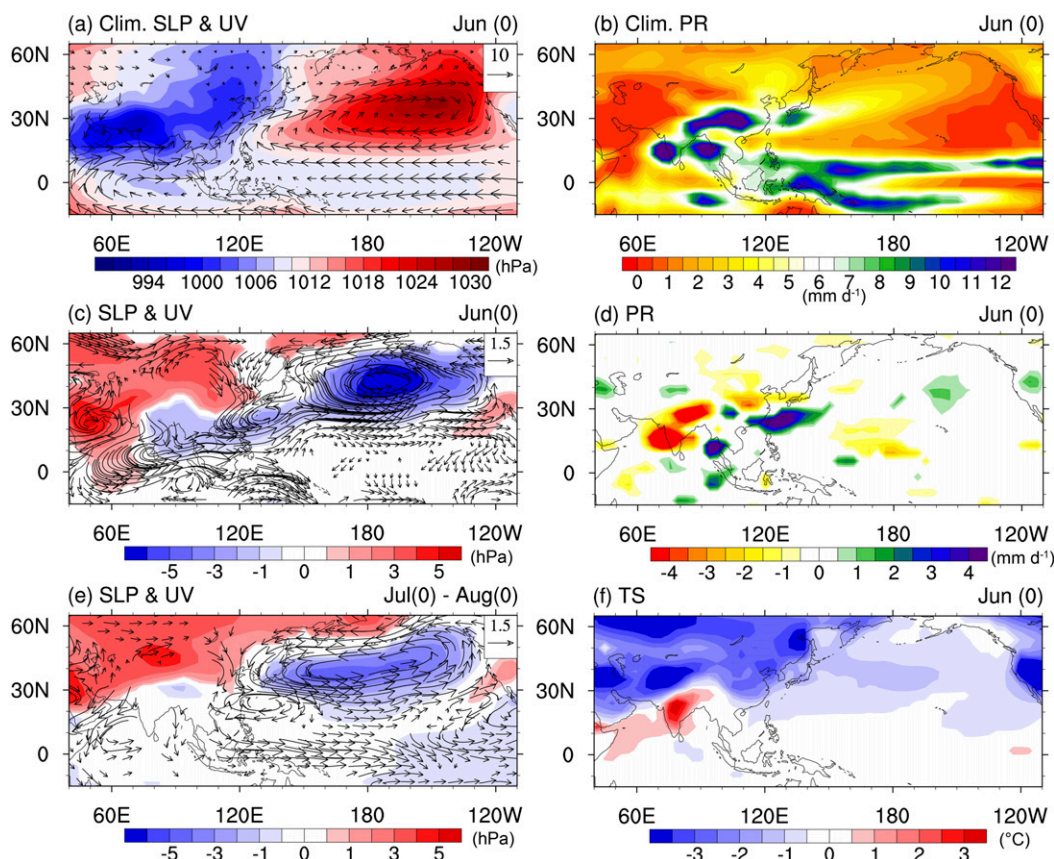
FIG. 9. (a) Climatological sea level pressure anomalies (shading; hPa), 850-hPa wind anomalies (vectors; m s^{-1}), and (b) precipitation (mm day^{-1}) during June. (c),(e) Anomalous sea level pressure and 850-hPa winds during June (0) and July (0)–August (0), respectively, in the JAN experiment. (d),(f) Anomalous precipitation anomalies and surface temperature (°C) during June (0) in the JAN experiment. In (c)–(f), only the anomalies significant at the 5% test level are shown.

in three directions over the eastern Pacific, which causes the development of El Niño.

5. The impacts of the NHV eruptions on equatorial Pacific winds

Here we examine the ways in which the NHV eruptions affect the winds over the equatorial Pacific because the latter can trigger El Niño events. In particular, the NHV eruptions occurring in different seasons are expected to have differing impacts on the equatorial winds.

As shown in Fig. 9a, during June (0), the climatological land–sea contrast (warm land and cool ocean) induces the Asian low and North Pacific high (semipermanent systems) after the January eruption. The volcano-induced thermal contrast (relatively cold land and warm ocean) is opposite to the climatology, therefore, it tends to weaken the climatological Asian low and North Pacific high (or generate the high pressure anomalies over land and low pressure anomalies over

North Pacific and Asian marginal seas) (Fig. 9c). As a result, the anomalous North Pacific cyclone (NPC) develops and extends to the East and Southeast Asian marginal seas, combined with the weakened East Asian summer monsoon. Meanwhile, the volcano-induced midlatitude cooling is strong, especially over the arid regions of Iran and the Arabian Peninsula (Fig. 9f), which suppresses the South Asian summer monsoon precipitation (Fig. 9d). Since the climatological precipitation is large in India during June (Fig. 9b), the drier conditions enhance the downward shortwave radiation by reducing the cloud amount and reduce the upward latent heat flux, causing the surface warming (Fig. 9f). The low pressure anomalies are formed over India and the Bay of Bengal, connected with the low SLP over Southeast Asia. Then the anomalous cyclonic circulation is generated, and the anomalous westerlies appear over the equatorial Indo-western Pacific region.

After that, the anomalous high SLP in the JAN experiment becomes weaker over the midlatitude regions
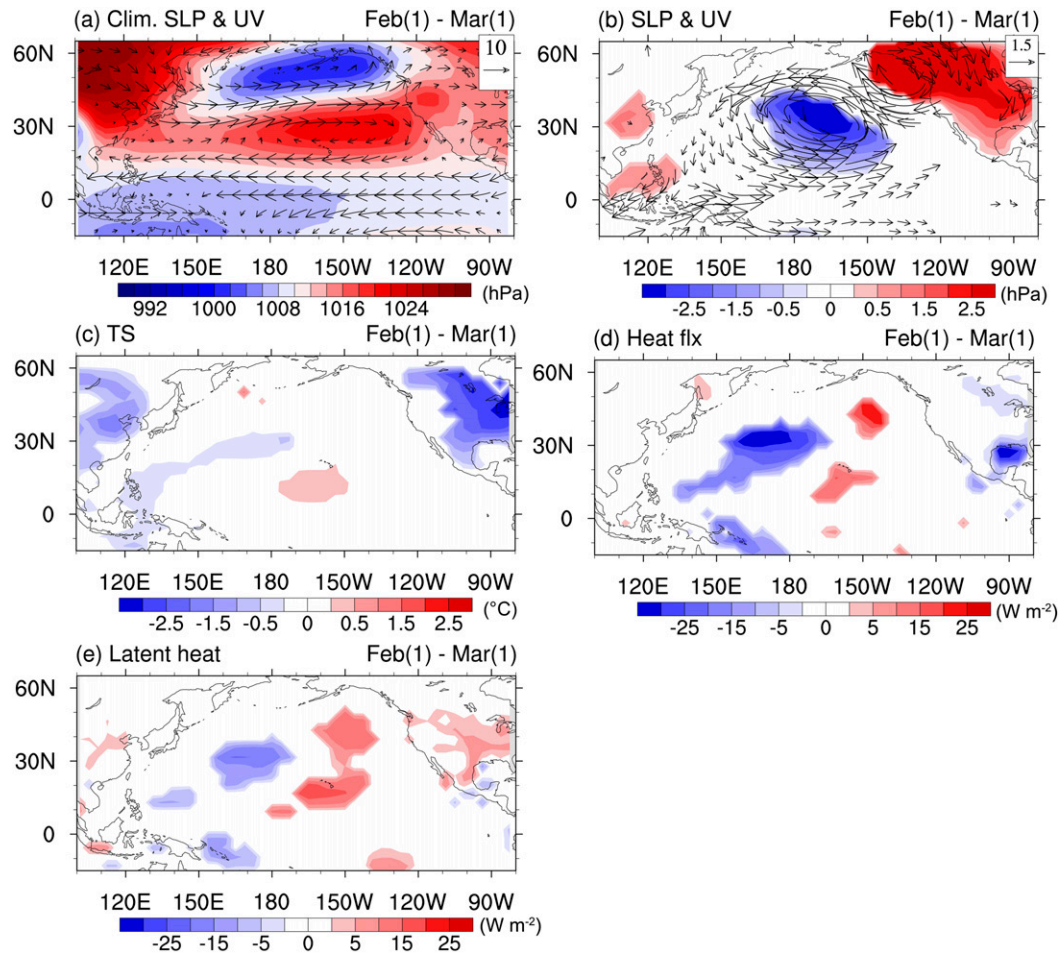
FIG. 10. (a) Climatological mean February–March sea level pressure (shading; hPa) and 850-hPa winds (vectors; m s^{-1}). (b) Composite sea level pressure anomalies and 850-hPa wind anomalies during February (1)–March (1) in the OCT experiment. (c) Composite surface temperature anomalies (°C), (d) surface downward heat flux anomalies (W m^{-2}), and (e) surface latent heat flux anomalies (W m^{-2}) during February (1)–March (1) in the OCT experiment. In (b)–(e), only the anomalies significant at the 5% test level are shown.

of Eurasia and the anomalous low SLP over the North Pacific and South Asia is also weakened (Fig. 9e), resulting in weaker anomalous westerlies appearing over the equatorial Indian Ocean. However, the anomalous westerlies-induced downwelling oceanic Kelvin waves have already propagated eastward and the ensuing Bjerknes feedback is in action and induces the weakened trade winds over the equatorial Pacific. This Bjerknes feedback results from the anomalous westerlies in the western Pacific during June (0) (Fig. 9c) and anomalous zonal advection of warm water from the western Pacific, which once in the central Pacific further slacken the equatorial trade winds.

In the October ensemble, the sulfate aerosols are mainly distributed in midlatitudes but they are weaker than January and April eruptions (Fig. 1d). Since cooling appears over the NH midlatitudes (Fig. 3d) and the

land–ocean thermal contrast is increased, the winter monsoon is enhanced over south East Asia during the February (1)–March (1) (Fig. 10b). The land–ocean thermal contrast strengthens the climatological Aleutian low and weakening subtropical North Pacific high (Fig. 10a), inducing an anomalous NPC. This anomalous NPC connects with the enhanced East Asian winter monsoon over the South China Sea, reducing the surface temperature in Maritime Continent (Fig. 10d). Meanwhile, there is a dipole anomalous SST over the northern tropical Pacific, which is caused by the atmospheric circulation (Vimont et al. 2001). The enhanced total wind speed over the western North Pacific induces the upward latent heat flux (Figs. 10d,e), which causes the ocean to cool. The anomalous westerlies over the subtropical central North Pacific decrease the total wind speed and increase the downward latent heat flux,
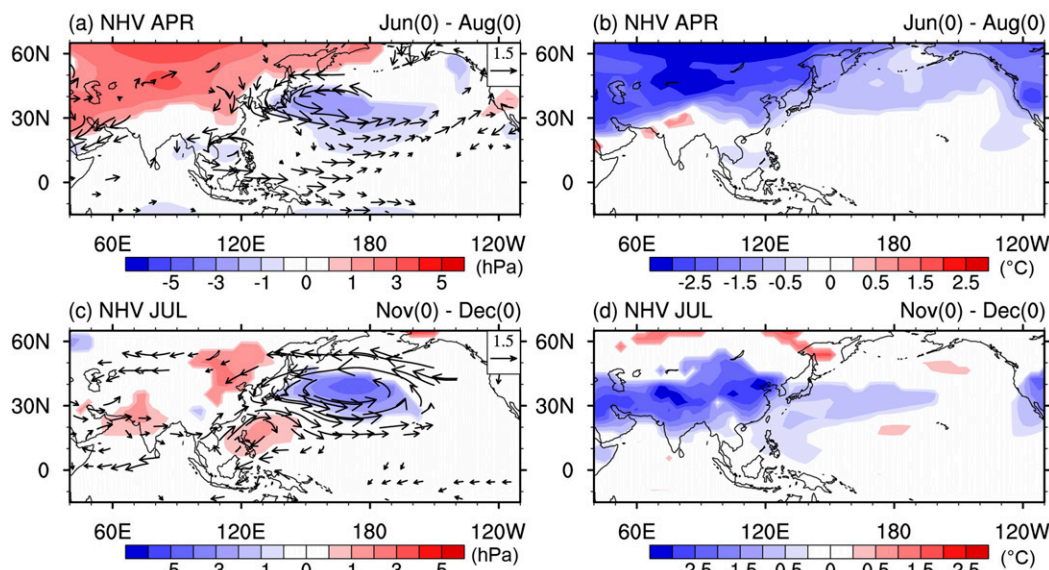
FIG. 11. Composite sea level pressure anomalies (hPa) and 850-hPa wind anomalies (vectors; m s^{-1}), and surface temperature (°C) during (a),(b) June (0)–August (0) in the APR experiment and (c),(d) November (0)–December (0) in the JUL experiment. Only the anomalies significant at the 5% test level are shown.

leading to the SST warming. Then the temperature gradient from the Maritime Continent to the subtropical central North Pacific is generated, exciting the anomalous equatorial westerlies over the western Pacific (Fig. 10b). The equatorial Pacific is very sensitive to equatorial winds (Emile-Geay and Cane 2009), so the Bjerknes feedback is activated to reduce the trade wind over the equatorial Pacific after early spring (1) (Fig. 8d).

In the April ensemble, aerosols are less intense over the midlatitudes (Fig. 1b), leading to a relatively lower cooling amplitude in summer (0) (Fig. 11b) compared to the January ensemble. The resultant anomalous high SLP over the midlatitude Eurasia and low SLP over the North Pacific are weak, which leads to a weak anomalous NPC (Fig. 11a). Meanwhile, the decline of the Asian summer monsoon is weak, which fails to generate an anomalous cyclone and connects with the NPC. Thus, the anomalous westerlies are very weak over the equatorial Pacific in summer (0).

After the July eruption, anomalous cooling over the Philippine Sea induces a local anomalous high SLP, along with northwesterly anomalies of NPC near 25°N, generating a western North Pacific anomalous anticyclone (WNPAC), due to a positive thermodynamic feedback between the anticyclone, convection, and underlying SST (Wang et al. 1999; Wang et al. 2000). The WNPAC generates the equatorial easterly anomalies over the western Pacific and prevents the eastern Pacific warming.

6. Discussion

The performance of CESM has been verified by previous researchers (e.g., Wang et al. 2015; Otto-Bliesner et al. 2016; Ning et al. 2017; Sun et al. 2017). CESM is also found to have good performance in simulating ENSO evolution after volcanic eruptions, confirmed by the proxies and observed data (Liu et al. 2017; Stevenson et al. 2017; Sun et al. 2018). Nevertheless, some model biases still exist. The simulated ENSO position is shifted westward compared to observations, which is a common deficiency of the current coupled models (e.g., Capotondi et al. 2006; Wang et al. 2018). This might lead to the slower transition rate from El Niño to La Niña (Sun et al. 2018). In addition, most IPCC-class GCMs, including CESM, have been found to be overly sensitive to stratospheric aerosol loading (Stoffel et al. 2015), due to incomplete representations of stratospheric aerosol chemistry (LeGrande et al. 2016).

Pausata et al. (2016) examine ENSO response to the NHV eruptions via the NorESM1-M, assuming that the eruptions have a weak impact on El Niño's development when the aerosol loading occurs during boreal winter, which is somewhat different from our results. However, there are some uncertainties in both models, which may lead to different ENSO responses. This means that multimodel analysis should be conducted in future work.

ENSO's response to the initial conditions is checked under the January and October eruptions (Fig. S3). For the January eruption, the NHV-induced El Niño–like

warming can be found in all three initial conditions at the end of year (0) and the warming is stronger under the El Niño and neutral initial conditions. After the October eruption, the El Niño–like warming happens in year (1) and it is strongest under the El Niño initial conditions than under the neutral initial conditions. These results are similar to those obtained by Ohba et al. (2013) and Predybaylo et al. (2017) but different from Pausata et al. (2016). Further studies need more models and observations to confirm the ENSO response within each set of initial conditions.

We conduct an idealized experiment, which does not consider the influence of the seasonal changes of atmospheric circulation on volcanic forcing, in order to determine if the same dispersion of aerosol occurring in different seasons can lead to different ENSO responses. We added the JAN forcing starting in April, July, and October (Fig. S4) and we made five ensemble members in each experiment. The January volcanic eruption forcing is selected because it can induce large NH extratropical cooling (Fig. 5a). We found that the same volcanic forcing also leads to the different magnitude of NH extratropical cooling (Fig. S5a), which might be due to the different locations of direct sunlight in the different seasons leading to different amounts of shortwave radiation blocked by volcanic aerosols. Although the significant El Niño is excited in the APR2 and JUL2 experiment (Figs. S5d,e), we can still find that the stronger El Niño occurs in the JAN2 (OCT2) than that in the APR2 (JUL2) experiment, and the El Niño is stronger in the OCT2 than that in APR2 experiment, which is also consistent with our previous results (Fig. 5). This means that the increased strength of the volcanic forcing can enhance El Niño's development in each season, but the eruption season controls the different intensity between them.

We also conduct the NHV experiments with the prescribed SST (three ensemble members for the January and October eruptions) and check if the pure effect of the land temperature changes can induce the anomalous equatorial westerlies. In the JAN prescribed-SST experiment (Fig. S6a), the South Asian monsoon is substantially decreased and the NPC is generated. The anomalous westerlies occur over the equatorial Indian Ocean and southwestern equatorial Pacific (about 10°S–0°, 110°–150°E), but they are weaker than the results in the JAN experiment (Figs. S6b,c). This means that the ocean enhances the midlatitude cooling, which further suppresses the South Asian summer monsoon, enhancing the anomalous westerlies over South Asia and the equatorial Indo-western Pacific. In the OCT prescribed-SST experiment (Fig. S7a), although the anomalous NPC and enhanced East Asian winter monsoon occur,

the east–west temperature gradient is not formed over the northern tropical Pacific (about 0°–15°N, 120°E–150°W) because the SST will not change in the fixed ocean and the ocean cannot get the heat flux changes from the atmosphere.

Previous studies found that the NHV-induced NH extratropics cooling leads to a southward shift of the ITCZ (Pausata et al. 2015b, 2016; Stevenson et al. 2016), which weakens the easterly trade winds over the equator because the surface easterly winds are weakest under the ITCZ. We checked the "ITCZ shift" mechanism in our study. In the JAN experiment, increased precipitation occurs from September (0) to December (0) and the ITCZ slightly moves southward (Fig. S8a), but the eastern Pacific warming is already formed (Fig. 5c). In the OCT experiment, the ITCZ southward movement starts at June (1) (Fig. S8e) but the eastern Pacific warming has already happened before June (1) (Fig. 5f). These results imply that the ITCZ shift might not be the trigger of El Niño in this study, although it can be an important enhancement mechanism to El Niño's development. We also check the results in the NHV experiments with the prescribed SST, and there is no ITCZ shift over the Pacific (figure not shown). This might be due to the coarse resolution of the simulation in this study, and it is not clear if this coarse resolution could spatially resolve the small ITCZ shift.

Because of the lack of high-latitude volcanic eruption events, it is difficult to truly retrieve the transport of volcanic aerosols, especially for the eruptions at different seasons. The prescribed volcanic forcing used in this research is based on a simple numerical distribution program and ignores some climatic effects, such as the quasi-biennial oscillation (Gao et al. 2008). The same meridional transport and vertical distribution schemes based on tropical eruptions are applied to the mid- to high-latitude eruptions, which may introduce additional uncertainties. It should be noted that we focus on medium-sized volcanic eruptions (similar to Pinatubo) as a template in this study, but volcanic eruption can take various forms and other factors need to be taking into consideration as well in future studies. A recent work by Toohey and Sigl (2017) is a major advance over the dataset of Gao et al. (2008). Their data can be used in future studies if they specify the evolution of the plume, but the latter should ideally be simulated by GCMs with active stratospheric dynamics and chemistry. Meanwhile, the spread of volcanic aerosols needs to be dynamically linked to stratospheric circulation in the model.

7. Conclusions

This study investigates the impact of northern high-latitude volcanic eruptions on ENSO, based on ensemble

simulations with the Community Earth System Model. The following are the major findings:

1) The seasonality of atmospheric circulation influences the NHV aerosol dispersion, causing a stronger (weaker) Northern Hemisphere cooling after the January and April (July and October) eruptions. ENSO's response to the medium-sized NHV eruptions strongly depends on the eruption season and its seasonal differences are much larger than that under tropical eruptions (Stevenson et al. 2017). The January eruption results in an El Niño toward the end of the eruption year while an El Niño occurs in year (1) after the October eruption. No significant eastern Pacific warming occurs after the April (July) eruption.

2) A diagnostic analysis indicates that the development of El Niño is mainly attributed to the zonal, meridional advective, and thermocline feedbacks over the eastern Pacific. These feedbacks are triggered by volcano-induced equatorial westerly anomalies over the western Pacific.

3) The ways by which the NHV eruptions excite anomalous equatorial westerlies are found to vary with the eruption season. Anomalous NPC and Asian monsoon are key systems to excite anomalous westerlies, which are mainly caused by the NHV-induced midlatitude cooling and Eurasian continent–Pacific thermal contrast. After January eruption, the NPC develops in early summer and connects with the weakened Asian summer monsoon, inducing the anomalous equatorial westerlies over the Indo-western Pacific, activating the Bjerknes feedback. For the October eruption, the anomalous NPC and enhanced East Asian winter monsoon bring cold air to the Maritime Continent and warm the subtropical central North Pacific through the surface heat flux exchange, exciting the anomalous westerlies over the western Pacific.

4) The strong dependence on the seasonal timing of the high-latitude eruption suggests that this should be a critical element of data–model comparisons. That is, one cannot judge the quality of a simulation of the response to high-latitude volcanic forcing without taking the eruption season into consideration.

It is important to specify the eruption season and probably the background state of the atmosphere at eruption time. This is a tall order but should be kept in mind in paleoclimate data–model comparisons. These findings also provide us new knowledge about the prediction of abrupt climate change after northern high-latitude volcanic eruptions and the climate effects of Arctic geoengineering (Robock et al. 2008; Nalam et al.

2018). However, due to the lack of large high-latitude eruption events and observations, we are still in the early stages of understanding the general rules for NHV eruptions' climate impacts. Thus, we need to find more volcanic reconstructions and climate proxies to verify the model results in the future.

REFERENCES

Adams, J. B., M. E. Mann, and C. M. Ammann, 2003: Proxy evidence for an El Niño-like response to volcanic forcing. *Nature*, **426**, 274–278, https://doi.org/10.1038/nature02101.

Ammann, C. M., G. A. Meehl, W. M. Washington, and C. S. Zender, 2003: A monthly and latitudinally varying volcanic forcing dataset in simulations of 20th century climate. *Geophys. Res. Lett.*, **30**, 1657, https://doi.org/10.1029/2003GL016875.

Benjamini, Y., and Y. Hochberg, 1995: Controlling the false discovery rate: A practical and powerful approach to multiple testing. *J. Roy. Stat. Soc.*, **57B**, 289–300.

Bjerknes, J., 1969: Atmospheric teleconnections from the equatorial Pacific. *Mon. Wea. Rev.*, **97**, 163–172, https://doi.org/10.1175/1520-0493(1969)097<0163:ATFTEP>2.3.CO;2.

Cane, M. A., 1984: Modeling sea level during El Niño. *J. Phys. Oceanogr.*, **14**, 1864–1874, https://doi.org/10.1175/1520-0485(1984)014<1864:MSLDEN>2.0.CO;2.

Capotondi, A., A. Wittenberg, and S. Masina, 2006: Spatial and temporal structure of tropical Pacific interannual variability in 20th century coupled simulations. *Ocean Modell.*, **15**, 274–298, https://doi.org/10.1016/j.ocemod.2006.02.004.

Chen, L., T. Li, and Y. Yu, 2015: Causes of strengthening and weakening of ENSO amplitude under global warming in four CMIP5 models. *J. Climate*, **28**, 3250–3274, https://doi.org/10.1175/JCLI-D-14-00439.1.

——, ——, B. Wang, and L. Wang, 2017: Formation mechanism for 2015/16 super El Niño. *Sci. Rep.*, **7**, 2975, https://doi.org/10.1038/s41598-017-02926-3.

Choi, K.-Y., G. A. Vecchi, and A. T. Wittenberg, 2013: ENSO transition, duration, and amplitude asymmetries: Role of the nonlinear wind stress coupling in a conceptual model. *J. Climate*, **26**, 9462–9476, https://doi.org/10.1175/JCLI-D-13-00045.1.

Colose, C. M., A. N. LeGrande, and M. Vuille, 2016: Hemispherically asymmetric volcanic forcing of tropical hydroclimate during the last millennium. *Earth Syst. Dyn.*, **7**, 681–696, https://doi.org/10.5194/esd-7-681-2016.

Cook, E. R., and P. J. Krusic, 2004: North American Drought Atlas. Lamont-Doherty Earth Observatory and the National Science Foundation, http://iridl.ldeo.columbia.edu/SOURCES/.LDEO/.TRL/.NADA2004/.pdsi-atlas.html.

——, R. Seager, R. R. Heim, R. S. Vose, C. Herweijer, and C. Woodhouse, 2010: Megadroughts in North America: Placing IPCC projections of hydroclimatic change in a long-term palaeoclimate context. *J. Quat. Sci.*, **25**, 48–61, https://doi.org/10.1002/jqs.1303.

D'Arrigo, R., R. Seager, J. E. Smerdon, A. N. LeGrande, and E. R. Cook, 2011: The anomalous winter of 1783–1784: Was the Laki eruption or an analog of the 2009–2010 winter to blame? *Geophys. Res. Lett.*, **38**, L05706, https://doi.org/10.1029/2011GL046696.

Emile-Geay, J., and M. A. Cane, 2009: Pacific decadal variability in the view of linear equatorial wave theory. *J. Climate*, **39**, 203–219, https://doi.org/10.1175/2008JPO3794.1.

——, R. Seager, M. A. Cane, E. Cook, and G. H. Haug, 2008: Volcanoes and ENSO over the past millennium. *J. Climate*, **21**, 3134–3148, https://doi.org/10.1175/2007JCLI1884.1.

——, and Coauthors, 2016: Links between tropical Pacific seasonal, interannual and orbital variability during the Holocene. *Nat. Geosci.*, **9**, 168–173, https://doi.org/10.1038/ngeo2608.

Gao, C., A. Robock, and C. Ammann, 2008: Volcanic forcing of climate over the past 1500 years: An improved ice core–based index for climate models. *J. Geophys. Res.*, **113**, D23111, https://doi.org/10.1029/2008JD010239.

Grieser, J., and C. D. Schönwiese, 1999: Parameterization of spatiotemporal patterns of volcanic aerosol induced stratospheric optical depth and its climate radiative forcing. *Atmósfera*, **12**, 111–133.

Guo, S., G. J. S. Bluth, W. I. Rose, I. M. Watson, and A. J. Prata, 2004: Re-evaluation of SO$_2$ release of the 15 June 1991 Pinatubo eruption using ultraviolet and infrared satellite sensors. *Geochem. Geophys. Geosyst.*, **5**, Q04001, https://doi.org/10.1029/2003GC000654.

Hu, J., J. Emile-Geay, and J. Partin, 2017: Correlation-based interpretations of paleoclimate data—Where statistics meet past climates. *Earth Planet. Sci. Lett.*, **459**, 362–371, https://doi.org/10.1016/j.epsl.2016.11.048.

Khodri, M., and Coauthors, 2017: Tropical explosive volcanic eruptions can trigger El Niño by cooling tropical Africa. *Nat. Commun.*, **8**, 778, https://doi.org/10.1038/s41467-017-00755-6.

Kravitz, B., and A. Robock, 2011: Climate effects of high-latitude volcanic eruptions: Role of the time of year. *J. Geophys. Res.*, **116**, D01105, https://doi.org/10.1029/2010JD014448.

——, and Coauthors, 2015: The Geoengineering Model Intercomparison Project Phase 6 (GeoMIP6): Simulation design and preliminary results. *Geosci. Model Dev.*, **8**, 3379–3392, https://doi.org/10.5194/gmd-8-3379-2015.

Kunsch, H. R., 1989: The jackknife and the bootstrap for general stationary observations. *Ann. Stat.*, **17**, 1217–1241, https://doi.org/10.1214/aos/1176347265.

LeGrande, A. N., K. Tsigaridis, and S. E. Bauer, 2016: Role of atmospheric chemistry in the climate impacts of stratospheric volcanic injections. *Nat. Geosci.*, **9**, 652–655, https://doi.org/10.1038/ngeo2771.

Li, J., and Coauthors, 2013: El Niño modulations over the past seven centuries. *Nat. Climate Change*, **3**, 822–826, https://doi.org/10.1038/nclimate1936.

Li, T., Y. Zhang, E. Lu, and D. Wang, 2002: Relative role of dynamic and thermodynamic processes in the development of the Indian Ocean dipole: An OGCM diagnosis. *Geophys. Res. Lett.*, **29**, 2110, https://doi.org/10.1029/2002GL015789.

Lim, H.-G., S.-W. Yeh, J.-S. Kug, Y.-G. Park, J.-H. Park, R. Park, and C.-K. Song, 2016: Threshold of the volcanic forcing that leads the El Niño–like warming in the last millennium: Results from the ERIK simulation. *Climate Dyn.*, **46**, 3725–3736, https://doi.org/10.1007/s00382-015-2799-3.

Liu, F., J. Chai, B. Wang, J. Liu, X. Zhang, and Z. Wang, 2016: Global monsoon precipitation responses to large volcanic eruptions. *Sci. Rep.*, **6**, 24331, https://doi.org/10.1038/srep24331.

——, J. Li, B. Wang, J. Liu, T. Li, G. Huang, and Z. Wang, 2017: Divergent El Niño responses to volcanic eruptions at different latitudes over the past millennium. *Climate Dyn.*, **50**, 3799–3812 3799–3812, https://doi.org/10.1007/s00382-017-3846-z.

Liu, J., B. Wang, M. A. Cane, S.-Y. Yim, and J.-Y. Lee, 2013: Divergent global precipitation changes induced by natural versus anthropogenic forcing. *Nature*, **493**, 656–659, https://doi.org/10.1038/nature11784.

Maher, N., S. McGregor, M. H. England, and A. Sen Gupta, 2015: Effects of volcanism on tropical variability. *Geophys. Res. Lett.*, **42**, 6024–6033, https://doi.org/10.1002/2015GL064751.

Man, W. M., T. J. Zhou, and J. H. Jungclaus, 2014: Effects of large volcanic eruptions on global summer climate and East Asian monsoon changes during the last millennium: Analysis of MPI-ESM simulations. *J. Climate*, **27**, 7394–7409, https://doi.org/10.1175/JCLI-D-13-00739.1.

Mann, M. E., M. A. Cane, S. E. Zebiak, and A. Clement, 2005: Volcanic and solar forcing of the tropical Pacific over the past 1000 years. *J. Climate*, **18**, 447–456, https://doi.org/10.1175/JCLI-3276.1.

McGregor, S., and A. Timmermann, 2011: The effect of explosive tropical volcanism on ENSO. *J. Climate*, **24**, 2178–2191, https://doi.org/10.1175/2010JCLI3990.1.

——, ——, and O. Timm, 2010: A unified proxy for ENSO and PDO variability since 1650. *Climate Past*, **6**, 1–17, https://doi.org/10.5194/cp-6-1-2010.

Nalam, A., G. Bala, and A. Modak, 2018: Effects of Arctic geoengineering on precipitation in the tropical monsoon regions. *Climate Dyn.*, **50**, 3375–3395, https://doi.org/10.1007/s00382-017-3810-y.

Neale, R. B., J. Richter, S. Park, P. H. Lauritzen, S. J. Vavrus, P. J. Rasch, and M. Zhang, 2013: The mean climate of the Community Atmosphere Model (CAM4) in forced SST and fully coupled experiments. *J. Climate*, **26**, 5150–5168, https://doi.org/10.1175/JCLI-D-12-00236.1.

Ning, L., and R. S. Bradley, 2015: Influence of eastern Pacific and central Pacific El Niño events on winter climate extremes over the eastern and central United States. *Int. J. Climatol.*, **35**, 4756–4770, https://doi.org/10.1002/joc.4321.

——, and ——, 2016: NAO and PNA influences on winter temperature and precipitation over the eastern United States in CMIP5 GCMs. *Climate Dyn.*, **46**, 1257–1276, https://doi.org/10.1007/s00382-015-2643-9.

——, J. Liu, and W. Sun, 2017: Influences of volcano eruptions on Asian Summer Monsoon over the last 110 years. *Sci. Rep.*, **7**, 42626, https://doi.org/10.1038/srep42626.

——, ——, Z. Wang, and R. S. Bradley, 2018: Different influences on the tropical Pacific SST gradient from natural and anthropogenic forcing. *Int. J. Climatol.*, **38**, 2015–2028, https://doi.org/10.1002/joc.5313.

Ohba, M., H. Shiogama, T. Yokohata, and M. Watanabe, 2013: Impact of strong tropical volcanic eruptions on ENSO simulated in a coupled GCM. *J. Climate*, **26**, 5169–5182, https://doi.org/10.1175/JCLI-D-12-00471.1.

Oman, L., A. Robock, G. Stenchikov, G. A. Schmidt, and R. Ruedy, 2005: Climatic response to high latitude volcanic eruptions. *J. Geophys. Res.*, **110**, D13103, https://doi.org/10.1029/2004JD005487.

——, ——, G. L. Stenchikov, and T. Thordarson, 2006a: High-latitude eruptions cast shadow over the African monsoon and the flow of the Nile. *Geophys. Res. Lett.*, **33**, L18711, https://doi.org/10.1029/2006GL027665.

——, ——, ——, ——, D. Koch, D. T. Shindell, and C. Gao, 2006b: Modeling the distribution of the volcanic aerosol cloud from the 1783–1784 Laki eruption. *J. Geophys. Res.*, **111**, D12209, https://doi.org/10.1029/2005JD006899.

Otto-Bliesner, B. L., and Coauthors, 2016: Climate variability and change since 850 CE: An ensemble approach with the Community Earth System Model. *Bull. Amer. Meteor. Soc.*, **97**, 735–754, https://doi.org/10.1175/BAMS-D-14-00233.1.

Pausata, F. S. R., A. Grini, R. Caballero, A. Hannachi, and Ø. Seland, 2015a: High-latitude volcanic eruptions in the Norwegian Earth System Model: The effect of different initial conditions and of the ensemble size. *Tellus*, **67B**, 26728, https://doi.org/10.3402/tellusb.v67.26728.

——, L. Chafik, R. Caballero, and D. S. Battisti, 2015b: Impacts of high-latitude volcanic eruptions on ENSO and AMOC. *Proc. Natl. Acad. Sci. USA*, **112**, 13 784–13 788, https://doi.org/10.1073/pnas.1509153112.

——, C. Karamperidou, R. Caballero, and D. S. Battisti, 2016: ENSO response to high-latitude volcanic eruptions in the Northern Hemisphere: The role of initial conditions. *Geophys. Res. Lett.*, **43**, 8694–8702, https://doi.org/10.1002/2016GL069575.

Philander, S. G. H., 1985: El Niño and La Niña. *J. Atmos. Sci.*, **42**, 2652–2662, https://doi.org/10.1175/1520-0469(1985)042<2652:ENALN>2.0.CO;2.

Predybaylo, E., G. L. Stenchikov, A. T. Wittenberg, and F. Zeng, 2017: Impacts of a Pinatubo-size volcanic eruption on ENSO. *J. Geophys. Res.*, **122**, 925–947, https://doi.org/10.1002/2016JD025796.

Rayner, N. A., D. E. Parker, E. B. Horton, C. K. Folland, L. V. Alexander, D. P. Rowell, E. C. Kent, and A. Kaplan, 2003: Global analyses of sea surface temperature, sea ice, and night marine air temperature since the late nineteenth century. *J. Geophys. Res.*, **108**, 4407, https://doi.org/10.1029/2002JD002670.

Robock, A., 2000: Volcanic eruptions and climate. *Rev. Geophys.*, **38**, 191–219, https://doi.org/10.1029/1998RG000054.

——, L. Oman, and G. L. Stenchikov, 2008: Regional climate responses to geoengineering with tropical and Arctic SO_2 injections. *J. Geophys. Res.*, **113**, D16101, https://doi.org/10.1029/2008JD010050.

Ropelewski, C. F., and M. S. Halpert, 1987: Global and regional scale precipitation patterns associated with the El Niño/Southern Oscillation. *Mon. Wea. Rev.*, **115**, 1606–1626, https://doi.org/10.1175/1520-0493(1987)115<1606:GARSPP>2.0.CO;2.

Saha, S., and Coauthors, 2006: The NCEP Climate Forecast System. *J. Climate*, **19**, 3483–3517, https://doi.org/10.1175/JCLI3812.1.

Sato, M., J. E. Hansen, M. P. McCormick, and J. B. Pollack, 1993: Stratospheric aerosol optical depths, 1850–1990. *J. Geophys. Res.*, **98**, 22 987–22 994, https://doi.org/10.1029/93JD02553.

Shindell, D. T., G. A. Schmidt, M. E. Mann, and G. Faluvegi, 2004: Dynamic winter climate response to large tropical volcanic eruptions since 1600. *J. Geophys. Res.*, **109**, D05104, https://doi.org/10.1029/2003JD004151.

Sigl, M., and Coauthors, 2015: Timing and climate forcing of volcanic eruptions for the past 2,500 years. *Nature*, **523**, 543–549, https://doi.org/10.1038/nature14565.

Stenchikov, G. L., I. Kirchner, A. Robock, H.-F. Graf, J. C. Antuña, R. G. Grainger, A. Lambert, and L. Thomason, 1998: Radiative forcing from the 1991 Mount Pinatubo volcanic eruption. *J. Geophys. Res.*, **103**, 13 837–13 857, https://doi.org/10.1029/98JD00693.

Stevenson, S., B. Otto-Bliesner, J. Fasullo, and E. Brady, 2016: "El Niño like" hydroclimate responses to last millennium volcanic eruptions. *J. Climate*, **29**, 2907–2921, https://doi.org/10.1175/JCLI-D-15-0239.1.

——, J. T. Fasullo, B. L. Otto-Bliesner, R. A. Tomas, and C. Gao, 2017: Role of eruption season in reconciling model and proxy responses to tropical volcanism. *Proc. Natl. Acad. Sci. USA*, **114**, 1822–1826, https://doi.org/10.1073/pnas.1612505114.

Stoffel, M., and Coauthors, 2015: Estimates of volcanic-induced cooling in the Northern Hemisphere over the past 1500 years. *Nat. Geosci.*, **8**, 784–788, https://doi.org/10.1038/ngeo2526.

Su, J., R. Zhang, T. Li, X. Rong, J. Kug, and C.-C. Hong, 2010: Causes of the El Niño and La Niña amplitude asymmetry in the equatorial eastern Pacific. *J. Climate*, **23**, 605–617, https://doi.org/10.1175/2009JCLI2894.1.

——, T. Li, and R. Zhang, 2014: The initiation and developing mechanisms of central Pacific El Niños. *J. Climate*, **27**, 4473–4485, https://doi.org/10.1175/JCLI-D-13-00640.1.

Sun, W., J. Liu, and Z. Wang, 2017: Simulation of centennial-scale drought events over eastern China during the past 1500 years. *J. Meteor. Res.*, **31**, 17–27, https://doi.org/10.1007/s13351-017-6090-x.

——, ——, B. Wang, D. Chen, F. Liu, Z. Wang, L. Ning, and M. Chen, 2018: A "La Niña-like" state occurring in the second year after large tropical volcanic eruptions during the past 1500 years. *Climate Dyn.*, https://doi.org/10.1007/s00382-018-4163-x.

Thordarson, T., and S. Self, 2003: Atmospheric and environmental effects of the 1783–1784 Laki eruption: A review and reassessment. *J. Geophys. Res.*, **108**, 4011, https://doi.org/10.1029/2001JD002042.

Toohey, M., and M. Sigl, 2017: Volcanic stratospheric sulfur injections and aerosol optical depth from 500 BCE to 1900 CE. *Earth Syst. Sci. Data*, **9**, 809–831, https://doi.org/10.5194/essd-9-809-2017.

Ventura, V., C. J. Paciorek, and J. S. Risbey, 2004: Controlling the proportion of falsely rejected hypotheses when conducting multiple tests with climatological data. *J. Climate*, **17**, 4343–4356, https://doi.org/10.1175/3199.1.

Vimont, D. J., D. S. Battisti, and A. C. Hirst, 2001: Footprinting: A seasonal connection between the tropics and mid-latitudes. *Geophys. Res. Lett.*, **28**, 3923–3926, https://doi.org/10.1029/2001GL013435.

Wallace, J. M., and D. S. Gutzler, 1981: Teleconnections in the geopotential height field during the Northern Hemisphere winter. *Mon. Wea. Rev.*, **109**, 784–812, https://doi.org/10.1175/1520-0493(1981)109<0784:TITGHF>2.0.CO;2.

Wang, B., R. Wu, and R. Lukas, 1999: Roles of the western North Pacific wind variation in thermocline adjustment and ENSO

phase transition. *J. Meteor. Soc. Japan*, **77**, 1–16, https:// doi.org/10.2151/jmsj1965.77.1_1.

——, ——, and X. Fu, 2000: Pacific–East Asian teleconnection: How does ENSO affect East Asian climate? *J. Climate*, **13**, 1517–1536, https://doi.org/10.1175/1520-0442(2000)013<1517: PEATHD>2.0.CO;2.

Wang, T., D. Guo, Y. Gao, H. Wang, F. Zheng, Y. Zhu, J. Miao, and Y. Hu, 2018: Modulation of ENSO evolution by strong tropical volcanic eruptions. *Climate Dyn.*, **51**, 2433–2453, https://doi.org/10.1007/s00382-017-4021-2.

Wang, Z., Y. Li, B. Liu, and J. Liu, 2015: Global climate internal variability in a 2000-year control simulation with Community Earth System Model (CESM). *Chin. Geogr. Sci.*, **25**, 263–273, https://doi.org/10.1007/s11769-015-0754-1.

Webster, P. J., V. O. Magaña, T. N. Palmer, J. Shukla, R. A. Tomas, M. Yanai, and T. Yasunari, 1998: Monsoons: Processes, predictability, and the prospects for prediction. *J. Geophys. Res.*, **103**, 14 451–14 510, https://doi.org/10.1029/97JC02719.

Wu, Y.-K., L. Chen, C.-C. Hong, T. Li, C.-T. Chen, and L. Wang, 2018: Role of the meridional dipole of SSTA and associated cross-equatorial flow in the tropical eastern Pacific in terminating the 2014 El Niño development. *Climate. Dyn.*, **50**, 1625–1638, https://doi.org/10.1007/s00382-017-3710-1.